applied optics

Lidar remote sensing of the aquatic environment: invited

James H. Churnside[1,*] and Joseph A. Shaw[2]

[1]Chemical Sciences Division, NOAA Earth System Research Laboratory, 325 Broadway, Boulder, Colorado 80305, USA
[2]Electrical and Computer Engineering Department, Montana State University, P.O. Box 173780, Bozeman, Montana 59717, USA
*Corresponding author: james.h.churnside@noaa.gov

Received 8 October 2019; revised 6 November 2019; accepted 7 November 2019; posted 7 November 2019 (Doc. ID 379597); published 23 March 2020

This paper is a review of lidar remote sensing of the aquatic environment. The optical properties of seawater relevant to lidar remote sensing are described. The three main theoretical approaches to understanding the performance of lidar are considered (the time-dependent radiative transfer equation, Monte Carlo simulations, and the quasi-single-scattering assumption). Basic lidar instrument design considerations are presented, and examples of lidar studies from surface vessels, aircraft, and satellites are given.

https://doi.org/10.1364/AO.59.000C92

1. INTRODUCTION

As another review paper in this issue describes, passive remote sensing has had an enormous impact on our understanding of the ocean [1]. Measurement examples include global distributions of surface concentrations of chlorophyll [2–4] and particulate organic carbon [5–7]. With some modeling, net primary productivity can be found from either chlorophyll [8–10] or carbon [11–13] biomass. In addition, passive remote sensing has been successful at identifying harmful algal blooms [14–16].

Despite these and other successes, there are limitations to passive remote sensing. One obvious limitation of passive remote sensing in this application is that it cannot operate with insufficient sunlight (e.g., at night or at high latitudes [17]). This means that passive systems will miss the effects of diurnal vertical migration of phytoplankton [18–20] and of diurnal cycles of phytoplankton physiology that affect the optical properties [21–23]. Another limitation is that passive remote sensing can only provide a vertically averaged measurement that is heavily weighted toward the surface, with almost no response below the first optical depth. As a result, passive remote sensing does not provide information on the deep chlorophyll maximum and underestimates phytoplankton biomass and primary productivity [24–27]. Lidar can operate at night, at high latitudes, and can generally penetrate to the subsurface chlorophyll maximum.

In this paper, we consider lidar used for remote sensing of aquatic environments. This kind of lidar system transmits laser light and detects a small fraction of the light scattered by water and particles or other objects in the water (bathymetric lidar for mapping the bottom surface beneath the water is outside the scope of this paper). Also, we focus on incoherent lidar systems that record the scattered irradiance as opposed to coherent lidar systems that also determine the phase of the scattered light through coherent mixing with a local oscillator.

2. OPTICAL PROPERTIES OF THE OCEAN RELEVANT TO LIDAR PERFORMANCE

In general, the signal from an oceanographic lidar depends on the absorption, scattering, and fluorescence within the water column, as well as the reflection from the sea surface and bottom. Here we discuss some of those processes.

Absorption within the water column occurs in the water itself, in dissolved materials, and in organic and mineral particles. Figure 1 shows the spectral dependence of absorption for pure water, clear seawater, and less clear seawater. For pure water, the best measurements at wavelengths above 550 nm are those of Pope and Fry [28]. Below about 500 nm, more recent measurements of Mason *et al.* are more accurate [29]. Between 500 and 550 nm, the two measurements are virtually identical. These measurements show a minimum absorption in the ultraviolet. Even the clearest natural ocean waters contain other constituents, however, and these raise the minimum absorption and shift it to a longer wavelength [30]. In less clear waters, the situation is more complicated, but bio-optical models have been developed to provide some guidance for Case 1 waters, in which the optical properties are dominated by phytoplankton. As an example, Morel [31] suggested an equation, valid for wavelengths between 400 and 700 nm, given by

$$a(\lambda) = [a_w(\lambda) + 0.06a_c^{*'}(\lambda)C^{0.65}] \times [1 + 0.2\exp(-0.014(\lambda - 440))], \quad (1)$$

where λ is the wavelength in nanometers (nm), C is the chlorophyll concentration in milligrams per cubic meter (mg m^{-3}),

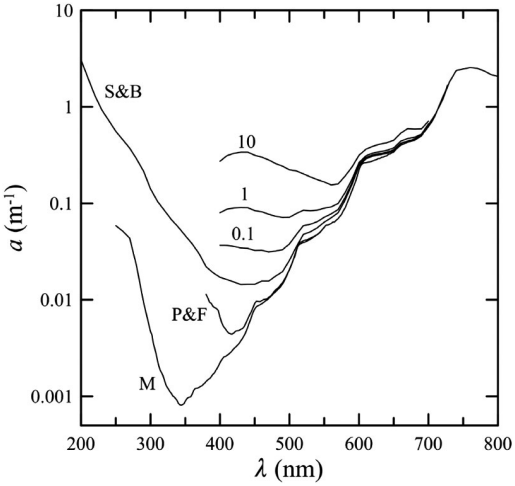

Fig. 1. Absorption coefficient of seawater a as a function of optical wavelength λ, including measurements of pure water by Pope and Fry (P&F) [28], more recent measurements at short wavelengths by Mason *et al.* (M) [29], measurements of very clear natural seawater by Smith and Baker (S&B) [30], and results of a bio-optical model for Case 1 waters with chlorophyll concentrations of 0.1, 1.0, and 10 mg m^{-3}.

and the two wavelength-dependent parameters have been published in tabular form [32,33].

The coefficient of scattering from pure seawater has been derived theoretically [34,35] and agrees within 2% of measured values [36]. It is slightly different from Rayleigh scattering and can be approximated by [33,37]

$$b_w = \left(1.64 \times 10^{-3} + 1.62 \times 10^{-5} S + 1.22 \times 10^{-6} T + 1.02 \times 10^{-7} TS\right) \left(\frac{532}{\lambda}\right)^{4.32}, \quad (2)$$

where S is salinity in practical salinity units (psu), T is temperature in °C, and λ is the optical wavelength in nm. For temperatures < 30°C, over 98% of this scattering is Brillouin scattering, and it is Doppler shifted from the initial laser frequency. For a nominal sound speed of 1500 m s^{-1} and a common wavelength of 532 nm, the shift is ±7.5 GHz. For seawater, the phase function, defined as the volume scattering function divided by the scattering coefficient, is given by [33]

$$\tilde{\beta}_w(\theta) = 0.06225(1 + 0.835\cos^2\theta), \quad (3)$$

where θ is the scattering angle. The backscattering coefficient, which includes all scattering for $\theta > 90°$, is given by $b_{bw} = 0.5 b_w$. For unpolarized light, scattering is uniform in all azimuthal angles. For polarized light, there is an azimuthal dependence that must be considered.

Particles in the ocean come in a wide variety of size, shape, and composition, so general statements about particulate scattering are much more difficult. Where the optical properties of the water are dominated by phytoplankton (Case 1 water), the particulate scattering coefficient can be approximated by [38]

$$b_p = 0.416 \frac{550}{\lambda} \text{chl}^{0.766}, \quad (4)$$

where chl is the chlorophyll concentration in mg m^{-3}. Measurements by Petzold [39] showed that the particulate phase function was similar for a wide variety of oceanic conditions. The backscattering ratio b_{bp}/b_p for these measurements was 0.0183, and the phase function can be approximated by a polynomial

$$\tilde{\beta}_p = \exp\big(-4.20799 - 2.91005\theta + 0.0909243\theta^2 + 0.563412\theta^3 + 0.353154\theta^4 + 0.108569\theta^5 + 0.0181941\theta^6 + 0.00159853\theta^7 + 0.0000579531\theta^8\big), \quad (5)$$

where θ is in radians. There have also been several analytical expressions suggested. The first, originally suggested for astrophysical applications by Henyey and Greenstein [40], is given by

$$\tilde{\beta}_p = \frac{1}{4\pi} \frac{1 - g^2}{[1 + g^2 - 2g\cos(\theta)]^{3/2}}, \quad (6)$$

where g is the anisotropy parameter. This function has the same backscattering ratio as the Petzold phase function for $g = 0.919$. Another analytical phase function, due to Fournier and Forand [41], is given by

$$\tilde{\beta}_p = \frac{\varepsilon(1-\delta) - (1-\delta^\varepsilon) + [\delta(1-\delta^\varepsilon) - v(1-\delta)]\sin^{-2}(0.5\theta)}{4\pi(1-\delta)^2\delta^\varepsilon} + \frac{1 - \delta_\pi^\varepsilon}{16\pi(\delta_\pi - 1)\delta_\pi^\varepsilon}[3\cos^2(\theta) - 1], \quad (7)$$

where

$$\varepsilon = \frac{3-\mu}{2}; \quad \delta_\pi = \frac{4}{3(n-1)^2}; \quad \delta = \delta_\pi \sin^2(0.5\theta). \quad (8)$$

Here μ is the slope of the particle size distribution, and n is the refractive index. The best fit to the Petzold data is for $n = 1.1$ and $\mu = 3.5835$. Finally, we present a polynomial fit to measurements of the phase function in the backscattering direction by Sullivan and Twardowski [42]:

$$\tilde{\beta}_p = 3.266 - 0.0815\theta + 8.007 \times 10^{-4}\theta^2 - 3.526 \times 10^{-9}\theta^3 + 5.885 \times 10^{-9}\theta^4, \quad (9)$$

where θ is in degrees. This phase function provided the best performance in radiative transfer calculations of ocean color [43]. These phase functions are presented in Fig. 2.

Because lidar measures the volume scattering function at 180°, the relationship between this parameter and the particulate backscattering coefficient must be known if information about the latter is desired. This relationship is characterized by the χ parameter, which is defined by

$$b_{bp} = 2\pi\chi(\pi)\beta_p(\pi). \quad (10)$$

Studies in both the field [42,44–47] and in the laboratory [45,48,49] have shown that the variability in χ is minimum at a scattering angle near 120°. Most studies report

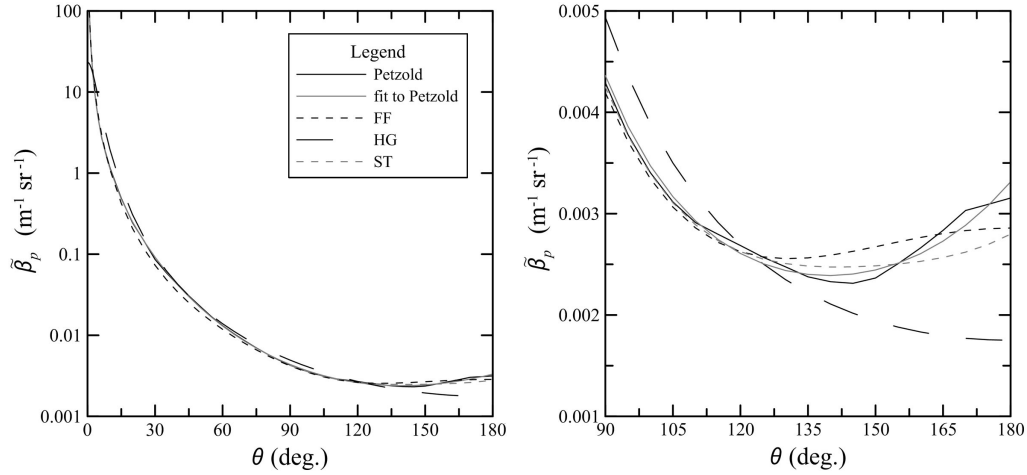

Fig. 2. Plot of several particulate phase functions $\tilde{\beta}_p$, including Petzold (solid black line), polynomial fit to Petzold (solid grey line), Fournier–Forand (FF; black short-dashed line), Henyey–Greenstein (HG; black long-dashed line), and Sullivan–Twardowski (ST; grey short-dashed line).

$\chi(120°) = 1.10 - 1.13$ with a variability of a few percent [42,44–48]. There is less agreement about the behavior of χ at larger scattering angles. Some studies reported lower values for $\chi(170°)$ [44,45,48], but most do not [42,45,47,48]. Two lidar measurements have been made, with estimates of $\chi(\pi) = 0.5$ [50] and $\chi(\pi) = 1.0$ [37].

Light also experiences Raman scattering from seawater and fluorescence from organic compounds, especially chlorophyll and other pigments associated with phytoplankton. Raman scattering has a much larger frequency shift (3400 cm^{-1}) than Brillouin scattering and a broader spectrum [51]. It also has a lower scattering coefficient of about 2.7×10^{-4} m^{-1} [51]. Fluorescence occurs at a number of wavelengths, including a strong line from the pigment chlorophyll-*a* at 685 nm. This peak has a width of about 25 nm and a quantum yield of a few percent [52]. Because of the high absorption at the fluorescence wavelength, lidar profiling is generally not attempted.

3. THEORETICAL LIDAR INVESTIGATIONS

The transfer of a polarized laser through a scattering and absorbing medium and back to the receiver can be expressed by the time-dependent radiative transfer equation [53,54]

$$\frac{1}{v}\frac{\partial \mathbf{I}(\mathbf{r}, \mathbf{s}, t)}{\partial t} + \mathbf{s} \cdot \nabla \mathbf{I}(\mathbf{r}, \mathbf{s}, t) + c\mathbf{I}(\mathbf{r}, \mathbf{s}, t) = b \int \mathbf{P}(\mathbf{s}, \mathbf{s}')[\mathbf{I}(\mathbf{r}, \mathbf{s}', t) - \mathbf{I}(\mathbf{r}, \mathbf{s}, t)]\mathrm{d}\mathbf{s}' + \mathbf{I}_0(\mathbf{r}, \mathbf{s}, t), \quad (11)$$

where $\mathbf{I}$ is the Stokes vector, $\mathbf{r}$ is the position vector, $\mathbf{s}$ is the direction vector, v is the speed of light in the propagation medium, c is the beam extinction coefficient, b is the scattering coefficient, $\mathbf{P}$ is the Mueller matrix, and $\mathbf{I}_0$ is the Stokes vector of the initial illumination. A common solution to this equation uses the discrete-ordinates method, in which the scattering phase function is expanded in a series of Legendre polynomials [33,55,56].

More commonly, a Monte Carlo approach has been used for lidar investigations. Early work considered detection of a target by an unpolarized lidar [57]. Gordon [58] used this approach to investigate the effects of multiple scattering on lidar attenuation. The technique was later extended to detection of fish schools [59] and subsurface layers [60]. The treatment of polarization in oceanographic lidar has been considered for oceanic water [61], for fish school detection [62], and for various idealized particle models [63]. Other recent work has considered methods to increase the speed of Monte Carlo calculations [64,65] and application of Monte Carlo to high-spectral-resolution lidar (HSRL) [66].

A simpler analysis makes use of the quasi-single-scattering approximation [67,68], which is based on the fact that most scattering in the ocean is contained in a small cone around the forward direction. The model is then a series of small-angle forward-scattering events, a single-scattering event near 180° to direct the light back toward the lidar, and another series of small-angle-scattering events on the path back to the lidar. Under this approximation, the lidar signals for co-polarized and cross-polarized returns can be written as [69]

$$S_C(z) = A_C \beta_C(\pi, z) \exp\left[-2\int_0^z \alpha(z')\mathrm{d}z'\right],$$

$$S_X(z) = \left\{A_X \beta_X(\pi, z) + 2A_X \beta_C(\pi, z)\int_0^z \gamma(z')\mathrm{d}z'\right\} \times \exp\left[-2\int_0^z \alpha(z')\mathrm{d}z'\right], \quad (12)$$

where S is the lidar signal, A is factor that includes lidar calibration and geometric losses, β is the volume backscattering coefficient, α is the lidar attenuation coefficient, and γ is the multiple-scattering depolarization coefficient. The subscript C refers to the co-polarized channel or co-polarized component of the volume backscattering, and the subscript X refers to the corresponding cross-polarized parameter. For a very narrow, highly collimated beam and receiver, α will be very nearly the beam attenuation coefficient c, and γ will be very nearly 0, resulting in the true single-scattering case. For a large beam and/or wide

field-of-view receiver, α will be very nearly the diffuse attenuation coefficient K_d, and γ may be nonzero. Note also that $\gamma = 0$ for an unpolarized receiver.

One of the main advantages of the quasi-single-scattering approximation is that it can guide retrievals of lidar data to obtain scattering and attenuation parameters. For example, we note that the attenuation coefficient is contained within an integral that acts as a low-pass filter. This leads to an approximate retrieval in which variability in α is neglected and variability in β is obtained directly [70,71]. The approximation also applies to HSRL, in which β is known in the Brillouin channel, and the profile of α can be measured by that channel.

We should note that the theoretical investigations that use the full phase function vary in which function was used. Of the 15 calculations in this section that used the full particulate phase function, four used measured values [58,60,61] (including Petzold [62,64]), four used Henyey and Greenstein [55,64–66], three used Mie calculations of scattering from a collection of spheres with various size distributions [54,57,59], two used Fournier and Forand [65,66], one used another function [56], and one used a two-term Henyey and Greenstein function [66].

4. LIDAR DESIGN

In most lidars, the receiver collects a fraction of the light with scattering angles near 180°, although it is also possible to design a bistatic instrument with the transmitter and receiver separated by a large distance to measure scattering angles significantly different from 180°.

Strictly speaking, monostatic lidars have collocated and coaxial transmitters and receivers. However, many lidar systems have separate transmit and receive optics that are positioned next to or very close to each other. Such systems are formally bistatic lidars because of the separate optical subsystems, but they are sometimes called monostatic and could be described as non-coaxial monostatic lidars (or even "biaxial" lidars). Bistatic systems can more easily provide high optical isolation between the transmitted beam and the much weaker received light but can limit the range over which the transmit and receive beams are overlapped and aligned. Monostatic lidars can be more compact because of the shared transmit-receive optical system.

Equation (12) does not include the effects of background light, which adds to the signal and limits the minimum detectable signal. To reduce background light, one would like to minimize the optical filter bandwidth and match the receiver field-of-view angle to the transmitted laser divergence angle. The transmitted beam can be expanded and collimated to reduce the diffraction-driven divergence angle, and a narrow receiver field of view means an interference filter with a narrow bandwidth can be used. However, a narrow field of view can produce much greater attenuation of the lidar signal [58,72].

A variation on the incoherent, direct-detection lidar systems described so far is a HSRL, which uses a narrow-linewidth laser to separately measure the large-particle scattering and the Doppler-shifted Brillouin scattering. This makes the system more complex but allows direct measurement of attenuation and backscattering without the requirement for absolute radiometric calibration of the receiver [71]. Figure 3 is a typical schematic layout of a dual-polarization HSRL lidar system

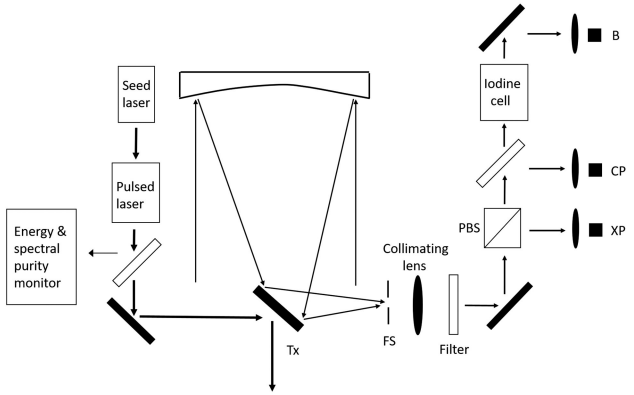

Fig. 3. Example HSRL configuration with iodine cell. A stable seed laser is locked to the iodine absorption at 532.293 nm, and an injection-seeded pulse laser creates a pulse at this wavelength to transmit into the ocean (Tx). The return light is collected by a telescope through a field-stop aperture (FS) to limit the receiver field of view. The light is recollimated and passed through an interference filter to limit the background light reaching the detectors. A polarization beamsplitter (PBS) directs the cross-polarized return to a detector (XP), a beamsplitter directs a portion of the co-polarized return to another detector (CP), and the remaining light is passed through an iodine filter to remove the particulate return and pass the Brillouin return to a third detector (B).

with an iodine absorption filter tuned to the laser wavelength to remove the particulate scattering in the Brillouin detection channel [50,73]. Generally, particulate scattering is much larger than Brillouin scattering, so a large fraction of the collected light has to be directed to the Brillouin channel to produce an acceptable signal-to-noise ratio in that channel. As a result, a high percentage of the collected light is absorbed in the iodine filter. To overcome this, a Michelson interferometer receiver has been developed to more effectively use the collected light [74,75]. The HSRL technique has only been used for aquatic lidar measurements since 2011, and all but one of the HSRL references cited here are since 2015. Of the experimental aquatic lidar papers cited here, approximately 16% refer to HSRL measurements, while the balance refer to conventional direct backscatter measurements.

The most common approach to incorporating polarization sensitivity into a lidar is to transmit a single linear or circular polarization state and to receive that state as the co-polarized signal and an orthogonal state as the cross-polarized signal. This can be done with a single receiver telescope followed by a polarization beam splitter that feeds the orthogonally polarized signals to separate detectors [50,76,77] or to separate telescopes for the co- and cross-polarized signals [69,78–80]. In the latter case, if the polarizers are not mounted on the front of the telescope, it is necessary to calibrate and account for the polarization sensitivity of the telescope and any optical components between it and the polarizer.

5. EXAMPLES OF LIDAR MEASUREMENTS

A wide variety of measurements have been made with oceanographic lidar on subsurface platforms, surface vessels, aircraft, and one satellite. Examples are presented below.

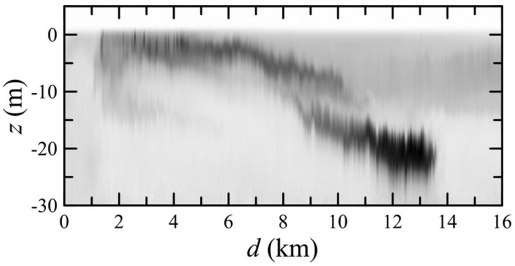

Fig. 4. Airborne lidar return as a function of depth z and distance along the flight track d. A stronger return is represented by darker grey. The return has been corrected for the effects of attenuation.

Surface and subsurface measurements have the advantage of proximity to supporting measurements. In 1978, a ship-based lidar was used to detect fish in cages [81]. Later, fish schools were measured by a lidar and echosounder on the same ship [82]. Subsurface scattering layers and signal fluctuations have also been measured [83,84], but most studies have concentrated on lidar attenuation and depolarization compared with *in situ* instrumentation [76,78,85]. One interesting result of this work is that the linear depolarization of the lidar signal was found to be related to the particulate backscatter ratio b_{bp}/b_p [76].

Airborne measurements have the advantage that large areas of the ocean can be covered quickly. One of the earliest applications was a demonstration of bathymetric measurements in Lake Ontario, USA in 1969. This application advanced rapidly, and there are several companies now making bathymetric lidars commercially. In 1972, an airborne lidar measured chlorophyll-*a* fluorescence in Lake Ontario [86]. The technique was improved by adding a receiver channel at the water Raman wavelength for calibration of the fluorescence signal [87,88] and by adding the measurement of dissolved organic material (DOM) [89].

Airborne lidar has also proven effective at detecting and mapping fish. The first reported detection was in 1977 [90], and comparisons between airborne lidar and traditional fisheries' techniques for a wide variety of species were reviewed in 2014 [72]. Since that review, airborne lidar has been used to map the distribution of flying fish in the Gulf of Mexico [91] and of lake trout in Yellowstone Lake, USA [79]. It also led to the discovery that jellyfish aggregations swim in vertical circles to maintain coherence, which produces aggregations that are hollow in the center [92].

Airborne lidar is particularly useful for mapping the depth distribution of phytoplankton (Fig. 4). This technique has demonstrated that thin plankton layers (1–5 m) are widespread [80,93–95]. Because these layers are often associated with a density gradient in the ocean, they can be used as tracers of internal wave propagation on the density gradient [96,97]. Even without such distinct layering, the vertical distribution of phytoplankton can provide useful information; two different species of harmful cyanobacteria in Lake Erie, USA can be identified by the differences in their characteristic depth profiles [98].

Most of the measurements to date have not been made with HSRL. The technique was first described in a 1991 patent [99]. The first ocean measurements used a system designed for the atmosphere, and its performance was limited by the 22.5 m depth resolution in water [100]. That design was reconfigured to allow better depth resolution and demonstrated good agreement with attenuation measurements from satellite-based ocean color [50]. The same system was used to measure spatial scales of variability in the ocean's optical properties [101]. Another study compared HSRL profiles with *in situ* measurements of K_d and b_{bp}, showing good agreement [73]. HSRL data have also been used to compare the performance of HSRL and an inversion using only the channel that includes scattering from all sources [71].

Satellite measurements have the advantage of true global coverage, although there are currently no oceanographic lidar systems in orbit. There is an orbiting atmospheric lidar, the Cloud-Aerosol Lidar with Orthogonal Polarization (CALIOP), with two orthogonal polarization receivers at 532 nm [77]. The sampling resolution of 22.5 m in water and the poor transient response of the detectors [102] make CALIOP ill-suited for ocean profiling. Despite this, some profiles have been measured in clear water [103,104]. There have also been studies using the integrated subsurface return to measure the horizontal distribution of plankton in the Arctic [17] and globally [105]. These results, along with airborne demonstrations, have provided the background for proposals for a true oceanographic lidar in space [106,107].

Other than bathymetric, fluorescence, and Raman measurements, all of the work above has used polarization. The cross-polarized lidar return only includes scattering from non-spherical particles, so fish, zooplankton, and large phytoplankton stand out more clearly against background-scattering levels in a cross-polarized lidar channel than a co-polarized channel. In addition, the ratio of cross- to co-polarization can provide some information about the scattering particles, with the largest ratios produced by large, irregularly shaped particles (e.g., fish).

6. CONCLUSIONS AND FUTURE DEVELOPMENTS

The main conclusion of this review is that oceanographic lidar is becoming an important tool to study the aquatic environment. Numerous examples have been provided using surface and airborne platforms.

We believe there are several exciting developments that will advance the utility of aquatic lidar. A blue laser source would provide much better depth penetration in the open ocean than the green laser that is typically used, and a commercially available instrument for measuring *in situ* scattering and polarization at 180° would provide badly needed ground-truth data. For non-HSRL systems, work is continuing on inversion techniques to better measure attenuation and backscattering with a single channel. For HSRL systems, higher pulse energy in lasers with high spectral purity will improve depth penetration, as will continued development of the Michelson interferometer receiver. There is also great potential for combining lidar with passive polarimetry [108] or even adding additional polarimetric capabilities beyond simple co- and cross-polarization detection to lidar systems. Overall, the most exciting development would be a space-based lidar for global coverage.

Funding. National Science Foundation (OIA- 1757351).

Acknowledgment. A portion of this material is based upon work supported by the National Science Foundation under Grant No. OIA- 1757351. Any opinions, findings and conclusions or recommendations expressed in this material are those of the author(s)and do not necessarily reflect the views of the National Science Foundation.

REFERENCES

1. S. Sathyendranath, "Passive review," Appl. Opt. (to be published).
2. J. E. O'Reilly, S. Maritorena, B. G. Mitchell, D. A. Siegel, K. L. Carder, S. A. Garver, M. Kahru, and C. McClain, "Ocean color chlorophyll algorithms for SeaWiFS," J. Geophys. Res. Oceans **103**, 24937–24953 (1998).
3. R. Johnson, P. G. Strutton, S. W. Wright, A. McMinn, and K. M. Meiners, "Three improved satellite chlorophyll algorithms for the Southern Ocean," J. Geophys. Res. Oceans **118**, 3694–3703 (2013).
4. R. J. Brewin, G. Dall'Olmo, S. Pardo, V. van Dongen-Vogels, and E. S. Boss, "Underway spectrophotometry along the Atlantic Meridional Transect reveals high performance in satellite chlorophyll retrievals," Rem. Sensing Environ. **183**, 82–97 (2016).
5. C. Le, X. Zhou, C. Hu, Z. Lee, L. Li, and D. Stramski, "A color-index-based empirical algorithm for determining particulate organic carbon concentration in the ocean from satellite observations," J. Geophys. Res. Oceans **123**, 7407–7419 (2018).
6. M. Stramska, "Particulate organic carbon in the global ocean derived from SeaWiFS ocean color," Deep-Sea Res. Part I **56**, 1459–1470 (2009).
7. D. Stramski, R. A. Reynolds, M. Kahru, and B. G. Mitchell, "Estimation of particulate organic carbon in the ocean from satellite remote sensing," Science **285**, 239–242 (1999).
8. R. Smith, R. Eppley, and K. Baker, "Correlation of primary production as measured aboard ship in southern California coastal waters and as estimated from satellite chlorophyll images," Mar. Biol. **66**, 281–288 (1982).
9. R. Eppley, E. Stewart, M. R. Abbott, and U. Heyman, "Estimating ocean primary production from satellite chlorophyll. Introduction to regional differences and statistics for the Southern California Bight," J. Plankton Res. **7**, 57–70 (1985).
10. M. J. Behrenfeld and P. G. Falkowski, "Photosynthetic rates derived from satellite-based chlorophyll concentration," Limnol. Oceanogr. **42**, 1–20 (1997).
11. M. J. Behrenfeld, E. Boss, D. A. Siegel, and D. M. Shea, "Carbon-based ocean productivity and phytoplankton physiology from space," Global Biogeochem. Cycles **19**, GB1006 (2005).
12. T. Westberry, M. J. Behrenfeld, D. A. Siegel, and E. Boss, "Carbon-based primary productivity modeling with vertically resolved photoacclimation," Global Biogeochem. Cycles **22**, GB2024 (2008).
13. D. A. Siegel, M. J. Behrenfeld, S. Maritorena, C. R. McClain, D. Antoine, S. W. Bailey, P. S. Bontempi, E. S. Boss, H. M. Dierssen, S. C. Doney, R. E. Eplee, Jr., R. H. Evans, G. C. Feldman, E. Fields, B. A. Franz, N. A. Kuring, C. Mengelt, N. B. Nelson, F. S. Patt, W. D. Robinson, J. L. Sarmiento, C. M. Swan, P. J. Werdell, T. K. Westberry, J. G. Wilding, and J. A. Yoder, "Regional to global assessments of phytoplankton dynamics from the SeaWiFS mission," Rem. Sensing Environ. **135**, 77–91 (2013).
14. T. T. Wynne, R. P. Stumpf, and T. O. Briggs, "Comparing MODIS and MERIS spectral shapes for cyanobacterial bloom detection," Journal of Remote Sensing **34**, 6668–6678 (2013).
15. R. P. Stumpf, "Applications of satellite ocean color sensors for monitoring and predicting harmful algal blooms," J. Hum. Ecol. Risk Assess. **7**, 1363–1368 (2001).
16. A. A. Kurekin, P. I. Miller, and H. J. Van der Woerd, "Satellite discrimination of Karenia mikimotoi and Phaeocystis harmful algal blooms in European coastal waters: merged classification of ocean colour data," Harmful Algae **31**, 163–176 (2014).
17. M. J. Behrenfeld, Y. Hu, R. T. O'Malley, E. S. Boss, C. A. Hostetler, D. A. Siegel, J. L. Sarmiento, J. Schulien, J. W. Hair, X. Lu, S. Rodier, and A. J. Scarino, "Annual boom-bust cycles of polar phytoplankton biomass revealed by space-based lidar," Nat. Geosci. **10**, 118–122 (2017).
18. J. J. Cullen and S. G. Horrigan, "Effects of nitrate on the diurnal vertical migration, carbon to nitrogen ratio, and the photosynthetic capacity of the dinoflagellate *Gymnodinium splendens*," Mar. Biol. **62**, 81–89 (1981).
19. R. B. Forward, "Light and diurnal vertical migration: photobehavior and photophysiology of plankton," in *Photochemical and Photobiological Reviews* (Springer, 1976), pp. 157–209.
20. D. Kamykowski and S. J. Zentara, "The diurnal vertical migration of motile phytoplankton through temperature gradients," Limnol. Oceanogr. **22**, 148–151 (1977).
21. M. D. DuRand and R. J. Olson, "Diel patterns in optical properties of the chlorophyte *Nannochloris* sp.: relating individual-cell to bulk measurements," Limnol. Oceanogr. **43**, 1107–1118 (1998).
22. H. Claustre, A. Bricaud, M. Babin, F. Bruyant, L. Guillou, F. Le Gall, D. Marie, and F. Partensky, "Diel variations in *Prochlorococcus* optical properties," Limnol. Oceanogr. **47**, 1637–1647 (2002).
23. C. Poulin, D. Antoine, and Y. Huot, "Diurnal variations of the optical properties of phytoplankton in a laboratory experiment and their implication for using inherent optical properties to measure biomass," Opt. Express **26**, 711–729 (2018).
24. L. Fernand, K. Weston, T. Morris, N. Greenwood, J. Brown, and T. Jickells, "The contribution of the deep chlorophyll maximum to primary production in a seasonally stratified shelf sea, the North Sea," Biogeochemistry **113**, 153–166 (2013).
25. K. Weston, L. Fernand, D. K. Mills, R. Delahunty, and J. Brown, "Primary production in the deep chlorophyll maximum of the central North Sea," J. Plankton Res. **33**, 1627–1628 (2011).
26. J. J. Cullen, "Subsurface chlorophyll maximum layers: enduring enigma or mystery solved?" Annu. Rev. Mar. Sci. **7**, 207–239 (2015).
27. J. L. Cullen, "The deep chlorophyll maximum: comparing vertical profiles of chlorophyll *a*," Fish. Aquat. Sci. **39**, 791–803 (1982).
28. R. M. Pope and E. S. Fry, "Absorption spectrum (380–700 nm) of pure water. II. Integrating cavity measurements," Appl. Opt. **36**, 8710–8723 (1997).
29. J. D. Mason, M. T. Cone, and E. S. Fry, "Ultraviolet (250–550 nm) absorption spectrum of pure water," Appl. Opt. **55**, 7163–7172 (2016).
30. R. C. Smith and K. S. Baker, "Optical properties of the clearest natural waters (200–800 nm)," Appl. Opt. **20**, 177–184 (1981).
31. A. Morel, "Light and marine photosynthesis: a spectral model with geochemical and climatological implications," Prog. Oceanogr. **26**, 263–306 (1991).
32. L. Prieur and S. Sathyendranath, "An optical classification of coastal and oceanic waters based on the specific absorption curves of phytoplankton pigments, dissolved organic matter, and other particulate materials," Limnol. Oceanogr. **26**, 671–689 (1981).
33. C. D. Mobley, *Light and Water: Radiative Transfer in Natural Waters* (Academic, 1994).
34. X. Zhang, L. Hu, and M.-X. He, "Scattering by pure seawater: effect of salinity," Opt. Express **17**, 5698–5710 (2009).
35. L. Hu, X. Zhang, and M. J. Perry, "Light scattering by pure seawater: effect of pressure," Deep-Sea Res. Part I **146**, 103–109 (2019).
36. K. S. Shifrin, *Physical Optics of Ocean Water*, AIP Translation Series (American Institute of Physics, 1988).
37. J. H. Churnside and R. D. Marchbanks, "Calibration of an airborne oceanographic lidar using ocean backscattering measurements from space," Opt. Express **27**, A536–A542 (2019).
38. A. Morel and S. Maritorena, "Bio-optical properties of oceanic waters: a reappraisal," J. Geophys. Res. Oceans **106**, 7163–7180 (2001).
39. T. J. Petzold, *Volume Scattering Functions for Selected Ocean Waters* (Scripps Institution of Oceanography, 1972).
40. L. C. Henyey and J. L. Greenstein, "Diffuse radiation in the galaxy," Astrophys. J. **93**, 70–83 (1941).
41. G. R. Fournier and J. L. Forand, "Analytic phase function for ocean water," Proc. SPIE **2258**, 194–201 (1994).

42. J. M. Sullivan and M. S. Twardowski, "Angular shape of the oceanic particulate volume scattering function in the backward direction," Appl. Opt. **48**, 6811–6819 (2009).
43. M. Twardowski and A. Tonizzo, "Ocean color analytical model explicitly dependent on the volume scattering function," Appl. Sci. **8**, 2684 (2018).
44. E. Boss and W. S. Pegau, "Relationship of light scattering at an angle in the backward direction to the backscattering coefficient," Appl. Opt. **40**, 5503–5507 (2001).
45. M. Chami, E. Marken, J. J. Stamnes, G. Khomenko, and G. Korotaev, "Variability of the relationship between the particulate backscattering coefficient and the volume scattering function measured at fixed angles," J. Geophys. Res. Oceans **111**, C05013 (2006).
46. J.-F. Berthon, E. Shybanov, M. E. G. Lee, and G. Zibordi, "Measurements and modeling of the volume scattering function in the coastal northern Adriatic Sea," Appl. Opt. **46**, 5189–5203 (2007).
47. X. Zhang, E. Boss, and D. J. Gray, "Significance of scattering by oceanic particles at angles around 120 degree," Opt. Express **22**, 31329–31336 (2014).
48. A. L. Whitmire, W. S. Pegau, L. Karp-Boss, E. Boss, and T. J. Cowles, "Spectral backscattering properties of marine phytoplankton cultures," Opt. Express **18**, 15073–15093 (2010).
49. T. Harmel, M. Hieronymi, W. Slade, R. Röttgers, F. Roullier, and M. Chami, "Laboratory experiments for inter-comparison of three volume scattering meters to measure angular scattering properties of hydrosols," Opt. Express **24**, A234–A256 (2016).
50. J. Hair, C. Hostetler, Y. Hu, M. Behrenfeld, C. Butler, D. Harper, R. Hare, T. Berkoff, A. Cook, J. Collins, N. Stockley, M. Twardowski, I. Cetinić, R. Ferrare, and T. Mack, "Combined atmospheric and ocean profiling from an airborne high spectral resolution lidar," EPJ Web Conf. **119**, 22001 (2016).
51. J. S. Bartlett, K. J. Voss, S. Sathyendranath, and A. Vodacek, "Raman scattering by pure water and seawater," Appl. Opt. **37**, 3324–3332 (1998).
52. S. Maritorena, A. Morel, and B. Gentili, "Determination of the fluorescence quantum yield by oceanic phytoplankton in their natural habitat," Appl. Opt. **39**, 6725–6737 (2000).
53. S. Chandrasekhar, *Radiative Transfer, International Series of Monographs on Physics* (Clarendon, 1950).
54. W. Cai, X. Ni, S. K. Gayen, and R. R. Alfano, "Analytical cumulant solution of the vector radiative transfer equation investigates backscattering of circularly polarized light from turbid media," Phys. Rev. E **74**, 056605 (2006).
55. Z. Jin and K. Stamnes, "Radiative transfer in nonuniformly refracting layered media: atmosphere-ocean system," Appl. Opt. **33**, 431–442 (1994).
56. K. Mitra and J. H. Churnside, "Transient radiative transfer equation applied to oceanographic lidar," Appl. Opt. **38**, 889–895 (1999).
57. G. W. Kattawar and G. N. Plass, "Time of flight lidar measurements as an ocean probe," Appl. Opt. **11**, 662–666 (1972).
58. H. R. Gordon, "Interpretation of airborne oceanic lidar: effects of multiple scattering," Appl. Opt. **21**, 2996–3001 (1982).
59. M. M. Krekova, G. M. Krekov, I. V. Samokhvalov, and V. S. Shamanaev, "Numerical evaluation of the possibilities of remote laser sensing of fish schools," Appl. Opt. **33**, 5715–5720 (1994).
60. G. M. Krekov, M. M. Krekova, and V. S. Shamanaev, "Laser sensing of a subsurface oceanic layer. I. Effect of the atmosphere and wind-driven sea waves," Appl. Opt. **37**, 1589–1595 (1998).
61. G. M. Krekov, M. M. Krekova, and V. S. Shamanaev, "Laser sensing of a subsurface oceanic layer. II. Polarization characteristics of signals," Appl. Opt. **37**, 1596–1601 (1998).
62. V. S. Shamanaev, "Detection of schools of marine fish using polarization laser sensing," Atmos. Ocean. Opt. **31**, 358–364 (2018).
63. P. G. Stegmann, B. Sun, J. Ding, P. Yang, and X. Zhang, "Study of the effects of phytoplankton morphology and vertical profile on lidar attenuated backscatter and depolarization ratio," J. Quant. Spectry. Radiative Transfer **225**, 1–15 (2019).
64. P. Chen, D. Pan, Z. Mao, and H. Liu, "Semi-analytic Monte Carlo radiative transfer model of laser propagation in inhomogeneous sea water within subsurface plankton layer," Opt. Laser Technol. **111**, 1–5 (2019).
65. P. Chen, D. Pan, Z. Mao, and H. Liu, "Semi-analytic Monte Carlo model for oceanographic lidar systems: lookup table method used for randomly choosing scattering angles," Appl. Sci. **9**, 48 (2018).
66. D. Liu, Y. Zhou, W. Chen, Q. Liu, T. Huang, W. Liu, Q. Chen, Z. Liu, P. Xu, X. Cui, X. Wang, C. Le, and C. Liu, "Phase function effects on the retrieval of oceanic high-spectral-resolution lidar," Opt. Express **27**, A654–A668 (2019).
67. L. Dolin and V. Savelev, "Characteristics of the backscattering signal during pulsed irradiation of a turbid medium by a narrow directed light beam (short narrow light pulse reflection from thick turbid medium with strong anisotropic scattering, obtaining backscattering signal power from unsteady transport equation solution)," Akademiia Nauk Sssr, Izvestiia, Fizika Atmosfery I Okeana **7**, 505–510 (1971).
68. H. R. Gordon, "Simple calculation of the diffuse reflectance of the ocean," Appl. Opt. **12**, 2803–2804 (1973).
69. J. H. Churnside, "Polarization effects on oceanographic lidar," Opt. Express **16**, 1196–1207 (2008).
70. J. H. Churnside and R. D. Marchbanks, "Inversion of oceanographic profiling lidars by a perturbation to a linear regression," Appl. Opt. **56**, 5228–5233 (2017).
71. J. Churnside, J. Hair, C. Hostetler, and A. Scarino, "Ocean backscatter profiling using high-spectral-resolution lidar and a perturbation retrieval," Remote Sens. **10**, 2003 (2018).
72. J. H. Churnside, "Review of profiling oceanographic lidar," Opt. Eng. **53**, 051405 (2014).
73. J. A. Schulien, M. J. Behrenfeld, J. W. Hair, C. A. Hostetler, and M. S. Twardowski, "Vertically-resolved phytoplankton carbon and net primary production from a high spectral resolution lidar," Opt. Express **25**, 13577–13587 (2017).
74. Z. Cheng, D. Liu, Y. Zhang, Y. Yang, Y. Zhou, J. Luo, J. Bai, Y. Shen, K. Wang, C. Liu, L. Su, and L. Yang, "Field-widened Michelson interferometer for spectral discrimination in high-spectral-resolution lidar: practical development," Opt. Express **24**, 7232–7245 (2016).
75. Z. Cheng, D. Liu, J. Luo, Y. Yang, Y. Zhou, Y. Zhang, L. Duan, L. Su, L. Yang, Y. Shen, K. Wang, and J. Bai, "Field-widened Michelson interferometer for spectral discrimination in high-spectral-resolution lidar: theoretical framework," Opt. Express **23**, 12117–12134 (2015).
76. B. L. Collister, R. C. Zimmerman, C. I. Sukenik, V. J. Hill, and W. M. Balch, "Remote sensing of optical characteristics and particle distributions of the upper ocean using shipboard lidar," Remote Sens. Environ. **215**, 85–96 (2018).
77. W. H. Hunt, D. M. Winker, M. A. Vaughan, K. A. Powell, P. L. Lucker, and C. Weimer, "CALIPSO lidar description and performance assessment," J. Atmos. Ocean. Technol. **26**, 1214–1228 (2009).
78. D. M. Allocca, G. D. Ludbrook, L. J. Mullen, T. H. Holloway, and V. M. Contarino, "Joint US-UK polarized lidar trial," in *Airborne and In-Water Imaging* (SPIE, 1999), pp. 174–184.
79. M. R. Roddewig, J. H. Churnside, F. R. Hauer, J. Williams, P. E. Bigelow, T. M. Koel, and J. A. Shaw, "Airborne lidar detection and mapping of invasive lake trout in Yellowstone Lake," Appl. Opt. **57**, 4111–4116 (2018).
80. A. P. Vasilkov, Y. A. Goldin, B. A. Gureev, F. E. Hoge, R. N. Swift, and C. W. Wright, "Airborne polarized lidar detection of scattering layers in the ocean," Appl. Opt. **40**, 4353–4364 (2001).
81. K. Fredriksson, B. Galle, K. Nyström, S. Svanberg, and B. Öström, *Marine Laser Probing: Results from a Field Test* (Chalmers Institute of Technology, 1979), Vol. **245**.
82. J. H. Churnside, J. J. Wilson, and V. V. Tatarskii, "Lidar profiles of fish schools," Appl. Opt. **36**, 6011–6020 (1997).
83. O. A. Bukin, A. Y. Major, A. N. Pavlov, B. M. Shevtsov, and E. D. Kholodkevich, "Measurement of the lightscattering layers structure and detection of the dynamic processes in the upper ocean layer by shipborne lidar," Int. J. Remote Sens. **19**, 707–715 (1998).
84. J. H. Churnside, V. V. Tatarskii, and J. J. Wilson, "Oceanographic lidar attenuation coefficients and signal fluctuations measured from a ship in the Southern California Bight," Appl. Opt. **37**, 3105–3112 (1998).

85. V. M. Contarino, J. Prentice, D. M. Allocca, T. J. Kane, M. A. London, B. M. Concannon, T. P. Curran, and L. J. Mullen, "Ocean water clarity measurement using shipboard lidar systems," Proc. SPIE **4488**, 106–114 (2002).
86. H. H. Kim, "New algae mapping technique by the use of an airborne laser fluorosensor," Appl. Opt. **12**, 1454–1459 (1973).
87. M. Bristow, D. Nielsen, D. Bundy, and R. Furtek, "Use of water Raman emission to correct airborne laser fluorosensor data for effects of water optical attenuation," Appl. Opt. **20**, 2889–2906 (1981).
88. K. J. Lee, Y. Park, A. Bunkin, R. Nunes, S. Pershin, and K. Voliak, "Helicopter-based lidar system for monitoring the upper ocean and terrain surface," Appl. Opt. **41**, 401–406 (2002).
89. F. E. Hoge, P. E. Lyon, C. W. Wright, R. N. Swift, and J. K. Yungel, "Chlorophyll biomass in the global oceans: airborne lidar retrieval using fluorescence of both chlorophyll and chromophoric dissolved organic matter," Appl. Opt. **44**, 2857–2862 (2005).
90. J. L. Squire and H. Krumboltz, "Profiling pelagic fish schools using airborne optical lasers and other remote sensing techniques," Mar. Technol. Soc. J. **15**, 29–31 (1981).
91. J. H. Churnside, R. J. D. Wells, K. M. Boswell, J. A. Quinlan, R. D. Marchbanks, B. J. McCarty, and T. T. Sutton, "Surveying the distribution and abundance of flying fishes and other epipelagics in the northern Gulf of Mexico using airborne lidar," Bull. Mar. Sci. **93**, 591–609 (2017).
92. J. H. Churnside, R. D. Marchbanks, P. L. Donaghay, J. M. Sullivan, W. M. Graham, and R. J. D. Wells, "Hollow aggregations of moon jellyfish (*Aurelia* spp.)," J. Plankton Res. **38**, 122–130 (2016).
93. F. E. Hoge, C. W. Wright, W. B. Krabill, R. R. Buntzen, G. D. Gilbert, R. N. Swift, J. K. Yungel, and R. E. Berry, "Airborne lidar detection of subsurface oceanic scattering layers," Appl. Opt. **27**, 3969–3977 (1988).
94. J. H. Churnside and P. L. Donaghay, "Thin scattering layers observed by airborne lidar," ICES J. Mar. Sci. **66**, 778–789 (2009).
95. H. Liu, P. Chen, Z. Mao, D. Pan, and Y. He, "Subsurface plankton layers observed from airborne lidar in Sanya Bay, South China Sea," Opt. Express **26**, 29134–29147 (2018).
96. J. H. Churnside, R. D. Marchbanks, J. H. Lee, J. A. Shaw, A. Weidemann, and P. L. Donaghay, "Airborne lidar detection and characterization of internal waves in a shallow fjord," J. Appl. Remote Sens. **6**, 063611 (2012).
97. J. H. Churnside and L. A. Ostrovsky, "Lidar observation of a strongly nonlinear internal wave train in the Gulf of Alaska," Int. J. Remote Sens. **26**, 167–177 (2005).
98. T. S. Moore, J. H. Churnside, J. M. Sullivan, M. S. Twardowski, A. R. Nayak, M. N. McFarland, N. D. Stockley, R. W. Gould, T. H. Johengen, and S. A. Ruberg, "Vertical distributions of blooming cyanobacteria populations in a freshwater lake from LIDAR observations," Rem. Sensing Environ. **225**, 347–367 (2019).
99. H. E. Sweeney, P. J. Titterton, and D. A. Leonard, "Method of remotely measuring diffuse attenuation coefficient of sea water," US patent 4986656 (22 January 1991).
100. E. Saiki, C. Weimer, and M. Stephens, "An investigation of high spectral resolution lidar measurements over the ocean," Proc. SPIE **8159**, 81590F (2011).
101. W. J. Moses, S. G. Ackleson, J. W. Hair, C. A. Hostetler, and W. D. Miller, "Spatial scales of optical variability in the coastal ocean: implications for remote sensing and *in situ* sampling," J. Geophys. Res. Oceans **121**, 4194–4208 (2016).
102. X. Lu, Y. Hu, Z. Liu, S. Zeng, and C. Trepte, "CALIOP receiver transient response study," Proc. SPIE **8873**, 887316 (2013).
103. X. Lu, Y. Hu, C. Trepte, S. Zeng, and J. H. Churnside, "Ocean subsurface studies with the CALIPSO spaceborne lidar," J. Geophys. Res. Oceans **119**, 4305–4317 (2014).
104. J. Churnside, B. McCarty, and X. Lu, "Subsurface ocean signals from an orbiting polarization lidar," Remote Sens. **5**, 3457–3475 (2013).
105. M. J. Behrenfeld, Y. Hu, C. A. Hostetler, G. Dall'Olmo, S. D. Rodier, J. W. Hair, and C. R. Trepte, "Space-based lidar measurements of global ocean carbon stocks," Geophys. Res. Lett. **40**, 4355–4360 (2013).
106. C. A. Hostetler, M. J. Behrenfeld, Y. Hu, J. W. Hair, and J. A. Schulien, "Spaceborne lidar in the study of marine systems," Annu. Rev. Mar. Sci. **10**, 121–147 (2018).
107. G. Chen, J. Tang, C. Zhao, S. Wu, F. Yu, C. Ma, Y. Xu, W. Chen, Y. Zhang, J. Liu, and L. Wu, "Concept design of the "Guanlan" science mission: China's novel contribution to space oceanography," Front. Mar. Sci. **6**, 194 (2019).
108. C. Jamet, A. Ibrahim, Z. Ahmad, F. Angelini, M. Babin, M. J. Behrenfeld, E. Boss, B. Cairns, J. Churnside, J. Chowdhary, A. B. Davis, D. Dionisi, L. Duforêt-Gaurier, B. Franz, R. Frouin, M. Gao, D. Gray, O. Hasekamp, X. He, C. Hostetler, O. V. Kalashnikova, K. Knobelspiesse, L. Lacour, H. Loisel, V. Martins, E. Rehm, L. Remer, I. Sanhaj, K. Stamnes, S. Stamnes, S. Victori, J. Werdell, and P.-W. Zhai, "Going beyond standard ocean color observations: lidar and polarimetry," Front. Mar. Sci. **6**, 251 (2019).